

# Study of the Stress State of a Dissimilar Metal Weld Due to Manufacturing and Operational Conditions

Bernadett Spisák<sup>1,2\*</sup>, Zoltán Bézi<sup>1</sup>, Szabolcs Szávai<sup>2,3</sup>

<sup>1</sup> Bay Zoltán Nonprofit Ltd. for Applied Research, Iglói street 2, H-3519 Miskolc, Hungary

<sup>2</sup> Institute of Energy Engineering and Chemical Machinery, Faculty of Mechanical Engineering, University of Miskolc, Egyetem street 1, H-3515 Miskolc-Egyetemváros, Hungary

<sup>3</sup> Institute of Machine and Product Design, Faculty of Mechanical Engineering, University of Miskolc, Egyetem street 1, H-3515 Miskolc-Egyetemváros, Hungary

\* Corresponding author, e-mail: [bernadett.spisak@bayzoltan.hu](mailto:bernadett.spisak@bayzoltan.hu)

Received: 09 August 2021, Accepted: 24 November 2021, Published online: 07 January 2022

## Abstract

Welding is accompanied by the presence of weld residual stresses, which in case of dissimilar metal welds even with post weld heat treatment cannot be removed completely therefore they should be considered when assessing possible welding defects. The measurement of residual stress in metal weld is a very complex procedure and also in the investigated case could not be carried out as it is the part of a working plant. However, by modelling these processes, the residual stresses and deformation of the components caused by this manufacturing method can be determined. It is important to calculate these values as accurately as possible to determine the maximum load capacity of the structure. The structure under examination was the dissimilar metal weld of a VVER-440 steam generator. 2D simulations were performed, where temperature and phase-dependent material properties were implemented. Different loading scenarios were considered in the numerical analysis. The results can be useful to determine the real loading conditions of a given component and can be used to predict stress corrosion crack initiation locations, as well as to evaluate the lifetime and failure mode prediction of welded joints.

## Keywords

finite element simulation, dissimilar metal weld, welding residual stress, PWHT, operational loads

## 1 Introduction

In several nuclear power plants, the dissimilar metal welds have proved to be a sensitive part of the structure. Numerous dissimilar metal weld (DMW) joints show a tendency of cracking. One of the causes was determined to be the stress corrosion cracking mechanism, where the dominating source of the driving force is the residual stresses in the DMWs. Up until 2018 there were 46 major service cases in operating pressurized water reactor (PWR) and boiling water reactor (BWR) caused by stress corrosion cracking (SCC) centered on DMWs [1–4]. An example of SCC in pressurized water reactors is the circumferential cracking of the Wolf Creek pressurizer nozzles which was discovered in October of 2006 [5]. As in case of DMWs the impact of thermal sensitization, residual stress and galvanic effects are combined therefore they are more sensitive to SCC, also heat affected zones (HAZs) along the fusion lines of the DMWs are more susceptible to SCC [6].

In order to evaluate the crack propagation rate and path the stress distribution needs to be calculated in this article the determination of the stresses is investigated. This includes not only the operating stresses but also the weld residual stresses. A considerable number of experimental tools are available to investigate the magnitude and distribution of welding residual stresses; however, many tests are required for the verification and, in the case of multi-pass DMWs in nuclear power plants, the analysis can be very difficult and time-consuming. Therefore, the usage of the finite element method to investigate the welding processes has become widely spread [7, 8]. However, it should be mentioned that the residual stresses are sensitive to the material and welding parameters for example. bead placement, multi-pass welding, cooling time, therefore their precise consideration is necessary.

An example is the DMW in the steam generator (SG) of the VVER-440 power plants which creates a connection

between the SG and the primary collector. Here an austenitic and ferritic steel is joined together, therefore buttering layers were applied to create a more stable weld. The heterogeneous welding process consists of the following steps. First, the buttering layers are implemented at the surface of the ferritic material, then a post weld heat treatment (PWHT) is carried out to minimize the residual stresses, finally the process is finished with the filler weld.

### 2 Background of the analysis

In the following simulations the previously listed processes are presented, whereas in the final step the operational loads were also considered. Four types of simulations are compared. In the first case, the welding simulation was omitted and only the operational loads were applied, in the second case the welding of the joint was considered in addition to the design conditions (in the results shown as weld without buttering layer), hereafter the complete welding process was simulated with the buttering layers (in the results shown as weld with buttering layer). Finally, in the fourth type, the PWHT of the buttering layer was considered in addition to the welding process (in the results illustrated as welding with creep). The results of these simulations are presented in this paper.

The examined DMW is located at the connection of the SG and the primary collector of the VVER-440 units. At this connection, a so-called "pocket" can be found where due to the lack of effective drainage a medium with a higher corrosion potential is located. Therefore, the presence of the corrosive medium and the stresses resulting from the difference between the thermal properties of austenitic and ferritic steel, as well as the operational loads, can lead to stress corrosion cracking. During the repair of the given DMW in one of the VVER-440 unit, the cracking shown in Fig. 1 was found. The cracking appeared at the boundary of the ferritic steel and the first buttering layer. The chemical compositions of the first and second buttering layers were examined by electron diffraction method, which revealed the dilution of the alloying elements [9]. These results show that the analysis of the DMWs is very important and necessary to determine the residual stresses due to the manufacturing processes.

### 3 Finite element simulation

The finite element simulation was carried out with the usage of MSC.Marc. As mentioned above, four types of simulation were created using the finite element method. The geometry was simplified, and an axisymmetric finite element model was created as shown in Fig. 2 with dimensions indicated.

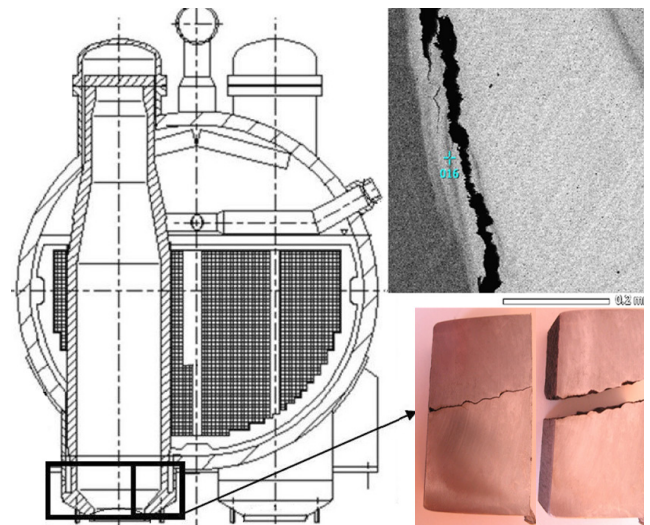


Fig. 1 Built-up of steam generator and crack found in the DMW [9]

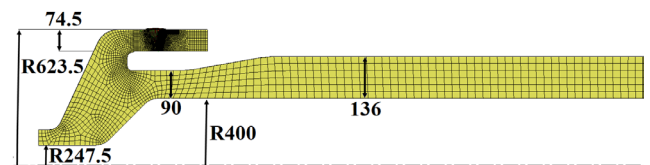


Fig. 2 Finite element model

In the model the steam generator was not built as it could not be simulated in 2D so the shortest distance of the connecting pipe was drawn, the primary collector was included thus the mechanical and thermal loading described in the following sections could be taken into account.

#### 3.1 Material properties

Several material properties are required to simulate dissimilar metal weld, considering not only the welding and PWHT, but also the working loads.

The structure altogether contains five materials, the base metals are the 22K ferritic steel and the 08H18N10T austenitic steel. The differences in material properties required the implementation of three buttering layers.

Two of them were from high alloyed EA-395/9 and one from EA-400/10T.

The joining weld was created with Sv-07Ch25N13 filler metal, for this in the simulation the 08H18N10T material properties were used. Their place in the geometry is presented in Fig. 3. The chemical compositions of the materials are listed in Table 1.

The material properties from the chemical compositions of the base metals were created using JMatPro software. For the ferritic steel and the buttering layers the temperature-dependent elastic-plastic isotropic hardening, and for the filler weld the phase-dependent material model was applied.

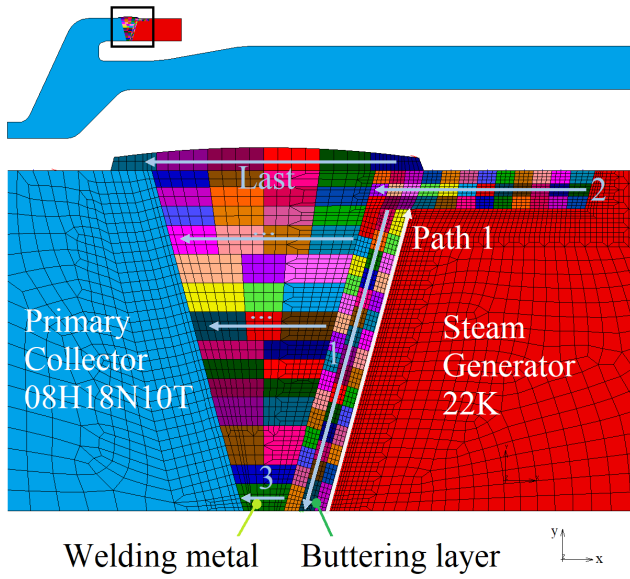


Fig. 3 Placement of the materials and weld passes

Table 1 Chemical compositions of the materials

Material	C (%)	Si (%)	Mn (%)	S (%)	P (%)	
22K	0.29	0.40	1.0	0.25	0.25	
EA-395/9	0.08	0.35	1.2	-	-	
EA-400/10T	0.07	0.5	1.5	-	-	
08H18N10T	0.08	0.08	1.5	0.02	0.035	
Material	Cr (%)	Ni (%)	Cu (%)	Co (%)	Mo (%)	Ti (%)
22K	0.30	0.30	0.30	0.02	-	-
EA-395/9	13.5	23	-	0.08	4.5	-
EA-400/10T	17	9.5	-	-	2	-
08H18N10T	17	9	-	-	-	0.4

For the 08H18N10T stainless steel, the strain hardening is considered with the usage of Chaboche's combined hardening law. It combines isotropic hardening, to describe the cyclic hardening or softening, and nonlinear kinematic hardening to capture proper characteristics of cyclic plasticity.

In MSC.Marc the von Mises yield criteria is defined by Eq. (1):

$$f = \sigma - (R + k), \quad (1)$$

where  $\sigma$  is the stress tensor. The main parameters of the isotropic hardening/softening are  $R$  and  $k$ . In the case of cyclic hardening, the initial conditions are  $k = \sigma_y$  and  $R = 0$ , while for the softening these are given as  $k = \sigma_y - R_0$  and  $R = R_0$ , where  $\sigma_y$  is the initial yield stress. The evolution equation for the variable is defined by Eq. (2):

$$\dot{R} = b(R_\infty - R)\dot{\lambda}, \quad (2)$$

where  $b$  and  $R_\infty$  are material constants and  $\dot{\lambda}$  is the equivalent plastic strain rate.  $R_\infty$  equals to the maximum change

in the size of the yield surface and  $b$  gives the rate at which the size of the yield surface changes as plastic strain develops. The nonlinear kinematic hardening can be determined from the linear-Ziegler rule by Eq. (3):

$$\dot{X} = \left[ \frac{C}{R+k} (\sigma - X) - \gamma X \right] \dot{\lambda}, \quad (3)$$

where  $C$  and  $\gamma$  are material constants. The applied parameters for steel 08H18N10T are shown in Table 2.

Further material properties are listed in Table 3, where  $\sigma_y$  is the yield stress,  $c$  is the specific heat capacity,  $\alpha$  is the thermal expansion coefficient and  $\lambda$  is the thermal conductivity. For the 22K steel phase dependent material properties were given, in the table the properties of the ferritic phase are shown.

The applied methodology of the modelling of dissimilar metal welds was validated in a previous research [8] where the welding of a DN 500 nozzles mock-up was simulated.

### 3.2 Welding process

Based on the welding procedure specification (WPS) the simulation contains 43 filler weld passes and 81 buttering weld passes. The layout of these weld beads are shown on Fig. 3. At first the welding of the three buttering layers was carried out and was followed with the joining weld. Between welding of the layers ~5 m in cooling time was considered. All of them were simulated with Goldak's double ellipsoid heat source shape (Fig. 4). The power density distribution for the front quadrant can be written down with Eq. (4) [10]:

$$q_f(x, y, z, t) = \frac{6\sqrt{3}f_r Q}{ba_f c\pi\sqrt{\pi}} e^{-\frac{3x^2}{b^2} - \frac{3y^2}{c^2} - 3(z+v(\tau-t))^2/a_f^2}. \quad (4)$$

In case of the rear quadrant a similar equation (Eq. (5)) can be used for the calculation of the power density distribution:

$$q_r(x, y, z, t) = \frac{6\sqrt{3}f_r Q}{ba_r c\pi\sqrt{\pi}} e^{-\frac{3x^2}{b^2} - \frac{3y^2}{c^2} - 3(z+v(\tau-t))^2/a_r^2}. \quad (5)$$

Table 2 Plasticity properties of 08H18N10T at room temperature

	$k$ (MPa)	$R_\infty$ (MPa)	$b$	$C$ (MPa)	$\gamma$
08H18N10T	270	300	50	1800	1.9

Table 3 Thermo-mechanical properties at 20 °C (\*ferritic phase)

	$E$ (GPa)	$\sigma_y$ (MPa)	$c$ (J/kg°C)	$\alpha$ ( $10^{-5}/^\circ\text{C}$ )	$\lambda$ (W/m°C)
22K*	208	251	447	1.28	44.34
08H18N10T	196	270	450	1.898	14.12
EA-395/9	212	365	434	1.623	11.95
EA-400/10T	203	420	443	1.831	13.46

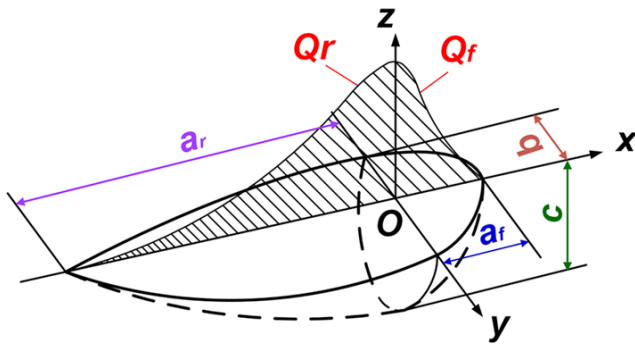


Fig. 4 Goldak's double ellipsoid heat source shape [10]

Where:

- $f_f$  is the fraction of the heat deposited in the front quadrant,
- $f_r$  is the fraction of the heat deposited in the rear quadrant,
- $\tau$  lag factor for defining the position of the source at time  $t = 0$ ,
- $v$  is the welding speed (m/s),
- $a_f, a_r, b, c$  are the parameters of the ellipsoidal heat source,
- $Q$  is the energy input rate (W), and calculated by Eq. (6):

$$Q = \eta UI. \tag{6}$$

Here  $\eta$  is the efficiency of the given welding process,  $\eta = 0.8$  in case of Shielded Metal Arc Welding (SMAW/111),  $U$  is the voltage and  $I$  is the current.

Also, it should be mentioned that  $f_f + f_r = 2$ , and the power density distribution inside the rear quadrant is lower than that in the front quadrant, therefore, the factor  $f_r$  is smaller than  $f_f$ .

From these equations it can be seen that for the simulation of welding the front length ( $a_f$ ), the rear length ( $a_r$ ), the width ( $b$ ) and the depth ( $c$ ) of the heat source has to be known. The depth and the width can be identified from a micrograph, the other values can be estimated with the following rules (Eq. (7) and Eq. (8)):

$$a_f = 0.6b \tag{7}$$

$$a_r = 2.0 \dots 2.5b. \tag{8}$$

If the micrograph of the welding is not known, then the so-called design throat can be used for the estimation of the other geometrical parameters. In this case the depth and the width of the heat source are given with Eq. (9) and Eq. (10):

$$d = a + 2.0 \dots 5.0 \text{ mm} \tag{9}$$

$$b = a + 1 \dots 2 \text{ mm}. \tag{10}$$

The heat source shape parameters were estimated based on the WPS, which are shown in Table 4 and Table 5. The value of the welding speed is approximately 4 mm/s.

Fig. 3 also shows the order of the welding, which is marked with blue arrows and is carried out in the following order:

- Welding of the buttering 1 (Fig. 3 1 weld path, from up to down)
- Welding of the buttering 2 (Fig. 3 2 weld path, from right to left)
- Welding of the filler weld (Fig. 3 from 3 to last weld path, from right to left and from down to up).

During the welding simulation, the surface heat losses were considered with the help of thermal edge films. For the radiation heat loss an emissivity coefficient of 0.8, and for the convective heat loss a heat transfer coefficient of 20 W/mK were given. Also in case of the inner side of the ferritic end of the component an equivalent boundary condition was applied according to the unmodelled ferritic region.

### 3.3 Modelling of the post weld heat treatment

There are several models to study the heat treatment process. Based on a large number of researches [3, 11–13] the creep model has the largest effect on the stress relief process. The time-dependent creep behavior can be divided into three parts: primary creep, secondary creep and

Table 4 Welding type and placement of the welds

	Welding run	Material	Welding process
Buttering 1	1–15	EA-395/9	111
	16–45	EA-400/10T	111
Buttering 2	1–11	EA-395/9	111
	12–36	EA-400/10T	111
Joining weld	1	08H18N10T	141
	2–43	08H18N10T	111

Table 5 Welding parameters of the buttering and the joint weld

	Current (A)	Voltage (V)	Type of Current and Polarity	Heat Input (kJ/mm)
Buttering 1	125–135	24–25	DCEP	~0.61
	140–150	25–26	DCEP	~0.69
Buttering 2	125–135	24–25	DCEP	~0.61
	140–150	25–26	DCEP	~0.69
Joint weld	70–80	24–25	DCEN	~0.61
	140–150	25–26	DCEP	~0.69

tertiary creep. The early rapid elongation occurs during primary creep thereafter the creep strain rate decreases and is propagated to secondary creep. In this phase, the creep strain rate becomes constant and finally, reaches the tertiary creep when the creep strain rate accelerates, and fracture occurs at the end of this phase.

In the case of post weld heat treatment, the material remains at an elevated temperature where creep can only occur for a short time, therefore the consideration of the third stage is not required.

There are numerous researches where the simulation of PWHT has been considered using a creep model, for example, Venkata et al. [13] and Dong et al. [3] use the Norton's steady-state creep model which for constant stress and temperature has the following formula (Eq. (11)):

$$\dot{\epsilon}_{cr} = A\sigma^n, \quad (11)$$

where  $\dot{\epsilon}_{cr}$  is the creep strain rate ( $s^{-1}$ ),  $A$  and  $n$  are temperature-dependent material constants, and the stress is in MPa.

Another version of this model is calculated from the Norton-Bailey Law, where time dependence is taken into account (Eq. (12)):

$$\dot{\epsilon}_{cr} = mA\sigma^n t^{m-1}, \quad (12)$$

where  $m$  is also a temperature-dependent material constant. This is called the strain hardening formulation for power-law creep. Since the time dependence of the model is necessary to account for PWHT process, therefore the second version of the Norton-Bailey Law presented in Eq. (12) was applied.

For the present simulation, creep data were not available for the materials E395/9 and EA400/10T used for the buttering layers, however, the properties of these materials are very similar to the joining metal, and therefore the required parameters for the Norton-Bailey creep model were calculated from creep diagrams found in the literature [14] for 08H18N10T steel using time-based bivariate regression analysis.

Equation (13) was used to determination  $m$  [15]:

$$m = \frac{k \sum_{i=1}^k (\ln t_i \ln \epsilon_i) - \sum_{i=1}^k (\ln t_i) \sum_{i=1}^k (\ln \epsilon_i)}{k \sum_{i=1}^k (\ln t_i)^2 - \left( \sum_{i=1}^k \ln t_i \right)^2}, \quad (13)$$

where  $k$  gives the number of points included in the regression analysis. Similarly,  $n$  was defined by Eq. (14):

$$n = \frac{k \sum_{i=1}^k (\ln \sigma_i \ln \epsilon_i) - \sum_{i=1}^k (\ln \sigma_i) \sum_{i=1}^k (\ln \epsilon_i)}{k \sum_{i=1}^k (\ln \sigma_i)^2 - \left( \sum_{i=1}^k \ln \sigma_i \right)^2}. \quad (14)$$

To determine the creep-strain coefficient,  $A$ , the previously determined constants  $m$  and  $n$  are used, and  $A$  can be calculated by Eq. (15):

$$A = e^{\frac{\sum_{i=1}^k (\ln \epsilon_i) - \sum_{i=1}^k (\sigma_i^n t_i^m)}{k}}. \quad (15)$$

Since the post weld heat treatment was carried out at 600 °C therefore the diagram shown in Fig. 5 from the [14] literature was used to determine the parameters. The calculated values are listed in Table 6.

For the heat up of the structure 500 minutes was used afterward the structure was kept at 600 °C for 960 minutes and finally the cooldown was carried out.

### 3.4 Operational loads and boundary conditions

After the welding simulation and PWHT, the boundary conditions for the operational loads were considered, where the pressure and temperature values were taken from the design conditions. These can be divided into two groups, thermal and mechanical loads.

Thermal loads were applied first. During the operation of the structure, the water in the primary circuit heats up the inner surface of the primary collector, at the same time the pocket is heated by the water in the secondary circuit. Finally, the temperature of the environment was also included on the outer surface of the steam generator.

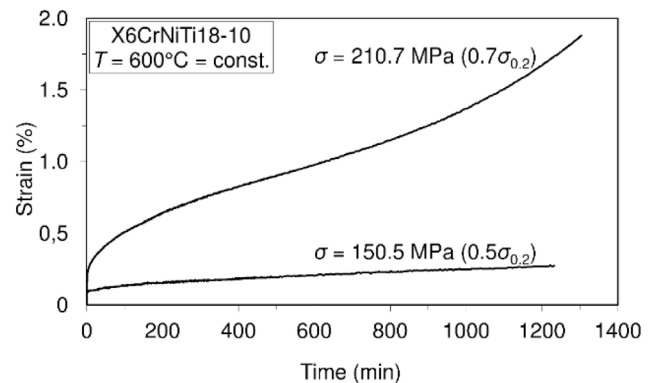


Fig. 5 Creep behavior of 08H18N10T at 600 °C [14]

Table 6 Parameters of the Norton-Bailey creep law at 600 °C

	$m$ [-]	$n$ [-]	$A$
08H18N10T	0.3395	4.5122	$5.60583 \times 10^{-14}$

The applied temperatures and heat transfer coefficients are listed in Table 7 and their placement is shown in Fig. 6.

The mechanical boundary conditions are shown in Fig. 7. From the beginning of the simulation the free side of the ferritic material was fixed. In case of the design conditions four additional loads were placed on the model:

- The pressure of the primary circuit acting on the inner side of the primary collector.
- The pressure of the secondary circuit, which is placed on the pocket.
- Compensated pressure at the end of the primary collector, to consider the effect of the pressure of the primary circuit on the axial tension.
- Compensated pressure at the end of the steam generator nozzle, to consider the effect of the pressure of the primary circuit and secondary circuit on the axial tension.

The values of the mechanical loads are listed in Table 8.

**Table 7** Thermal loads

Location	Temperature [°C]	Heat transfer coefficient [kW/m <sup>2</sup> °C]
The inner surface of the primary collector	325	4.2
Temperature of pocket	270	5.7
Temperature of environment	20	0.02

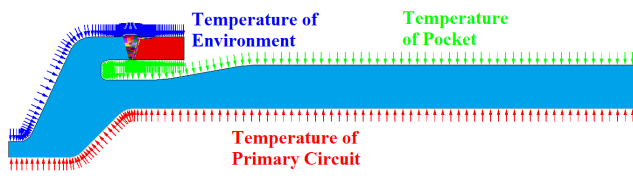


**Fig. 6** Temperature boundary conditions on the inner surface of the collector, the pocket and the environment

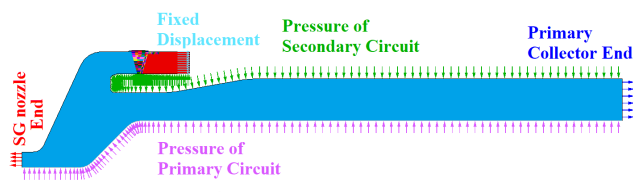


**Fig. 7** Pressure loads inside the primary collector and inside the SG and pressure loads at section ends to simulate axial stresses due to pressures

**Table 8** Pressure loads of the design conditions

Location	Pressure [MPa]
Primary circuit	14
Secondary circuit	6
End of the steam generator nozzle	-31.5
End of the primary collector	-10.1

#### 4 Modelling results

The purpose of this research was to estimate the effect of the operational loads and welding on the stresses, therefore the stress distribution is presented in more detail below. As it was already mentioned the DMWs in the steam generator of VVER-440 have a tendency of cracking at the interface of ferritic and austenitic material therefore the inspection of this part of the DMW was completed. In the presented diagrams (Fig. 8 and Fig. 9) the results along path 1 are included, the placement of pass 1 is shown in Fig. 3 with white color. The results are illustrated in cylindrical coordinate system, where the x axis represents the axial, the y axis the radial and the z axis the hoop orientation (Fig. 3). In the case of stress corrosion cracking, the most dangerous loads are tensile stresses. Fig. 9 shows the distribution of the axial stresses along path 1 where the 0 point of the x-axis represents the root side of the weld. As the diagram shows in case of the simulation without weld the stresses remain on low values also at the inner

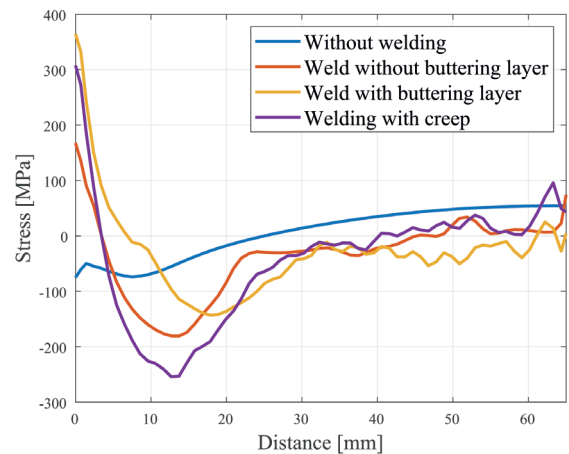


**Fig. 8** Through thickness variation of simulated axial stresses at the boundary of the ferritic base material and the buttering layer

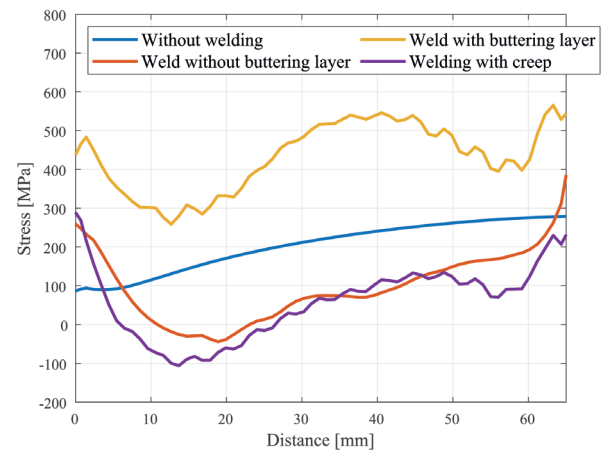


**Fig. 9** Through thickness variation of simulated hoop stress at the boundary of the ferritic base material and the buttering layer

side of the weld the stresses are in the negative range, whereas in case of the simulations with the inclusion of the welds at the root side large tensile stresses occur. In the second simulation, the welding under operating load was considered without simulation of the buttering layers.

As shown in the results, the axial stress on the root side of the weld reaches 170 MPa, and after about 4 mm it rapidly changes to compressive stress and remains there almost all the rest of the path 1. In case of the second, the third and the fourth simulation similar values occur for the axial stresses. The difference between the peak values of the third and fourth simulation is 58 MPa (365 MPa without creep, 307 MPa with creep), while in case of the second and fourth simulation it is 137 MPa. Therefore, it can be concluded that at the root side of the welding the analysis without the buttering layer underestimates the axial stress compared to the analysis with the inclusion of the post weld treatment (fourth case).

A larger difference can be seen for the hoop stresses along path 1 between the second and the third simulation, as shown in Fig. 9. However, the results of the second and the fourth analysis are analogous. Fig. 10 shows the changes in residual stresses before and after the post weld heat treatment, where the upper pictures show the axial stress and the lower pictures show the hoop stress distribution.

After the PWHT process, the values of axial and hoop tensile residual stresses are decreased due to the creep stress relaxation of the materials.

Fig. 11 presents the stress distribution of the axial stresses after the post weld heat treatment. The stress relief was carried out well, however, at the inner side of the weld the remaining tensile stress is still around 100 MPa. It has to be stated that the used Norton-Bailey creep model can achieve higher stress relaxation than the real one, as the model does not distinguish between primary

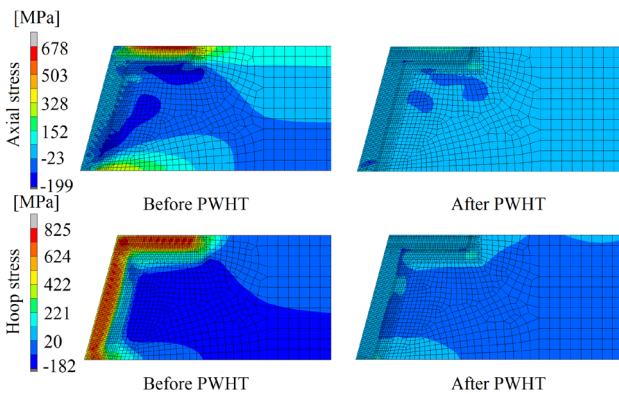


Fig. 10 Axial and hoop stress distribution before and after PWHT

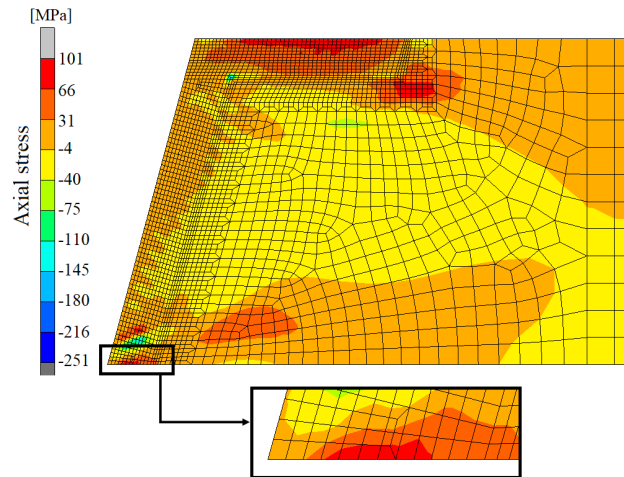


Fig. 11 Axial stress distribution after PWHT around the boundary of the ferritic metal and the buttering layer

and secondary creep, therefore relaxations obtained could be overestimated, resulting in even higher tensile stress in the pocket.

Fig. 12 displays the distribution of the axial stresses before and after the operational loads. It can be concluded that the simulation without welding does not reproduce the real residual stress distributions, much lower values were calculated. The result after welding shows that the stress distribution with and without the buttering layer procedure are similar, however at the root side of the boundary of the ferritic and austenitic steel some differences can be noticed, which impacts the final stress distribution, therefore it is necessary to include the simulation of PWHT.

An additional function of the model is the ability to predict the volume fraction of the different phases. At the beginning of the simulation the phase composition of the base materials before welding was 100% ferrite for the 22K steel and 100% austenite for the 08H18N10T steel. Fig. 13 shows the volume fraction of bainite due to phase transformations during the buttering weld process. Fig. 14 shows the volume fraction of ferrite where 1 means the steel is fully ferritic and 0 means has no ferritic phase fraction.

After the welding of the buttering layers on the ferritic side further phase changes will not occur, as the HAZ of the joining welding does not even reach the buttering layer closest to the ferritic steel.

In case of the joining welding only austenitic materials are welded therefore phase transformation will not occur.

The results emphasizes the necessity to incorporate the effects of phase transformation during the welding of buttering layers and the need to consider the effect of

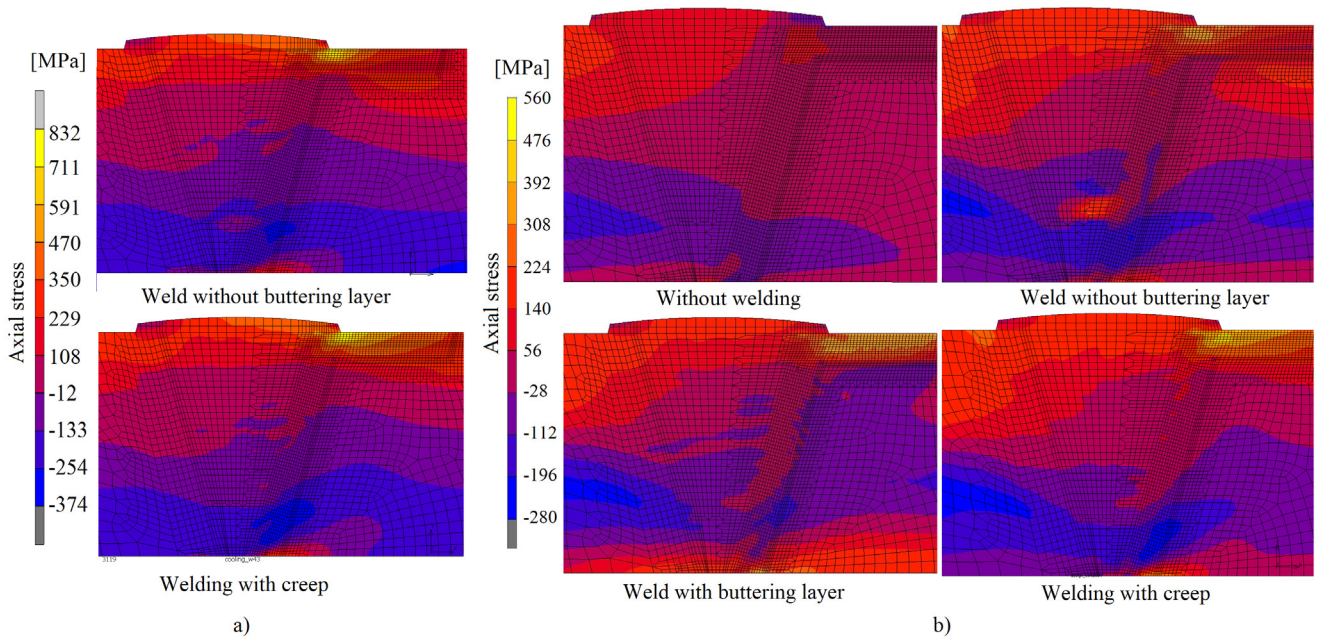


Fig. 12 Axial stress distribution a) after welding b) after operational loads

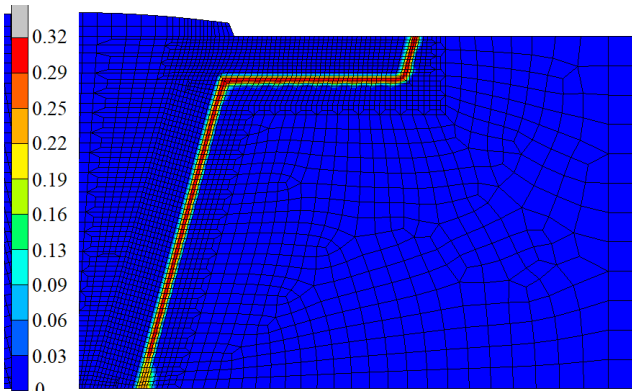


Fig. 13 Volume fraction of bainite

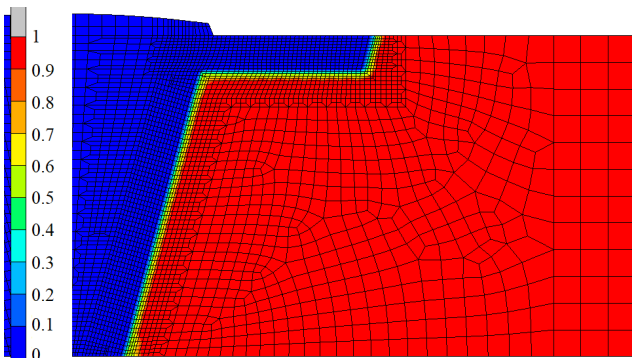


Fig. 14 Volume fraction of ferrite

stress relaxation during the post weld heat treatment in the mechanical analysis to predict the residual stresses accurately.

### 5 Conclusion

The numerical simulation of dissimilar weld in the steam generator of VVER-440 was performed in this research work. In the analysis, the effect of the buttering welds, the post weld heat treatment, the joint welds, and the operational loads were considered. From the results, the effect of the residual stresses on the final operating structure was determined. The following conclusions can be drawn from them:

1. The consideration of the buttering layer welding process can not be omitted from the simulation process and the PWHT process also has to be included to achieve more realistic results.
2. In the case of axial stresses, PWHT has a lower effect than for hoop stresses.
3. On the inner side of the weld, a large tensile axial residual stress appears at the boundary of the ferritic and austenitic material, which can lead to a high sensitivity to stress corrosion cracking.

## References

- [1] Dong, P., Brust, F. W. "Welding Residual Stresses and Effects on Fracture in Pressure Vessel and Piping Components: A Millennium Review and Beyond", *Journal of Pressure Vessel Technology*, 122(3), pp. 329–338, 2000.  
<https://doi.org/10.1115/1.556189>
- [2] International Atomic Energy Agency "Dissimilar Metal Weld Inspection, Monitoring and Repair Approaches", IAEA, Vienna, Austria, IAEA-TECDOC-1852, 2018.
- [3] Dong, W.-C., Gao, D.-B., Lu, S.-P. "Numerical Investigation on Residual Stresses of the Safe-End/Nozzle Dissimilar Metal Welded Joint in CAP1400 Nuclear Power Plants", *Acta Metallurgica Sinica (English Letters)*, 32(5), pp. 618–628, 2019.  
<https://doi.org/10.1007/s40195-018-0803-8>
- [4] Junek, L., Jurasek, L., Čančura, Z., Ernestová, M., Skoumalová, Z. "Degradation Mechanism of Dissimilar Metal Weld Joints on Steam Generator Collectors VVER 440MW Type", *Key Engineering Materials*, 741, pp. 134–137, 2017.  
<https://doi.org/10.4028/www.scientific.net/KEM.741.134>
- [5] Csontos, A. A., Rudland, D. L., Shim, D.-J., Xu, H., Wilkowski, G. "Flaw evaluation of Wolf Creek pressurizer nozzle indications", presented at 13th International Conference on Environmental Degradation of Materials in Nuclear Power Systems, Whistler, BC, Canada, Aug., 19–23, 2007.
- [6] Yeh, T.-K., Huang, G.-R., Wang, M.-Y., Tsai, C.-H. "Stress corrosion cracking in dissimilar metal welds with 304L stainless steel and Alloy 82 in high temperature water", *Progress in Nuclear Energy*, 63, pp. 7–11, 2013.  
<https://doi.org/10.1016/j.pnucene.2012.10.001>
- [7] Benson, M. L., Raynaud, P. A. C., Wallace, J. S. "Exploring finite element validation for weld residual stress prediction", In: *Proceedings of the ASME 2018 Pressure Vessels and Piping Conference*, Volume 6B: Materials and Fabrication, Prague, Czech Republic, 2018, Paper number: V06BT06A081.  
<https://doi.org/10.1115/PVP2018-84931>
- [8] Szávai, Sz., Bézi, Z., Ohms, C. "Numerical simulation of dissimilar metal welding and its verification for determination of residual stresses", *Frattura ed Integrità Strutturale*, 10(36), pp. 36–45, 2016.  
<https://doi.org/10.3221/IGF-ESIS.36.04>
- [9] Khodakov, V. D., Starchenko, E. G., Khodakov, D. V., Bazanov, M. A. "Анализ и исследование характера и причин повреждений сварных соединений №111(ПГВ-1000) и №23(ПГВ-440)" (Analysis and study of the nature and causes of damage to welded joints No. 111 (PGV-1000) and No. 23 (PGV-440)), [PowerPoint slides], ЦНИИТМАШ (СНИИТМАШ), Moscow, Russia, 2012. (in Russian)
- [10] Goldak, J., Chakravarti, A., Bibby, M. "A new finite element model for welding heat sources", *Metallurgical Transactions B*, 15(2), pp. 299–305, 1984.  
<https://doi.org/10.1007/BF02667333>
- [11] Jiang, J., Chiew, S. P., Lee, C. K., Tiong, P. L. Y. "A numerical study on residual stress of high strength steel box column", *Journal of Constructional Steel Research*, 128, pp. 440–450, 2017.  
<https://doi.org/10.1016/j.jcsr.2016.09.015>
- [12] Benson, M. L., Rudland, D. J., Csontos, A. "Weld Residual Stress Finite Element Analysis Validation: Part 1 – Data Development Effort", Office of Nuclear Regulatory Research, U.S. Nuclear Regulatory Commission, Washington, DC, USA, Rep. NUREG-2162, 2014.
- [13] Venkata, K. A., Kumar, S., Dey, H. C., Smith, D. J., Bouchard, P. J., Truman, C. E. "Study on the Effect of Post Weld Heat Treatment Parameters on the Relaxation of Welding Residual Stresses in Electron Beam Welded P91 Steel Plates", *Procedia Engineering*, 86, pp. 223–233, 2014.  
<https://doi.org/10.1016/j.proeng.2014.11.032>
- [14] Brnic, J., Turkalj, G., Canadija, M., Lanc, D., Krscanski S., Brcic, M., Li, Q., Niu, J. "Mechanical Properties, Short Time Creep, and Fatigue of an Austenitic Steel", *Materials*, 9(4), Article number: 298.  
<https://doi.org/10.3390/ma9040298>
- [15] May, D. L., Gordon, A. P., Segletes, D. S. "The Application of the Norton-Bailey Law for Creep Prediction Through Power Law Regression", In: *Proceedings of the ASME Turbo Expo 2013: Turbine Technical Conference and Exposition*, Volume 7A: Structures and Dynamics, San Antonio, Texas, USA, 2013, Paper number: V07AT26A005.  
<https://doi.org/10.1115/GT2013-96008>